RSC Sustainability

ROYAL SOCIETY OF CHEMISTRY

PAPER

View Article Online
View Journal



Cite this: DOI: 10.1039/d6su00100a

# Photoactivated histidine-modified ZnO nanostructures as esterase mimics: calcination-driven surface engineering for hydrolytic cleavage of bioactive esters

Swapan Patra,[a] Sounak Roy *[ab] and Nilanjan Dey *[a]

Zinc oxide (ZnO) nanocatalysts were synthesized *via* a co-precipitation route and thermally modulated at different calcination temperatures (300 °C and 700 °C) to elucidate the influence of thermal treatment on their physicochemical and catalytic properties. Comprehensive structural and surface analyses revealed that ZnO-300 possesses smaller crystallite size, higher surface area, and a three-dimensional nanoflake morphology enriched with abundant surface hydroxyl groups. In contrast, ZnO-700 forms a compact three-dimensional polyhedral structure with significantly reduced surface hydroxylation. The catalytic performance was systematically evaluated through the aqueous hydrolysis (pH 7.4) of a model acyl ester, *p*-nitrophenyl acetate (PNPA), and its long-chain analogue, *p*-nitrophenyl dodecanoate (PNPD). ZnO-300 exhibited superior catalytic efficiency, attributed to its enhanced surface area and higher density of surface hydroxyl groups. Furthermore, surface functionalization of ZnO-300 with histidine introduced Lewis acid–Brønsted base dual functionality and improved hydrophilicity, leading to enhanced hydrolytic activity. Under UV illumination, both ZnO-300 and histidine-modified ZnO (ZnO-His) showed pronounced photoactivation, with ZnO-His displaying the highest reactivity due to improved charge separation and radical-mediated pathways involving hydroxyl ($^{\bullet}OH$) and superoxide ($^{\bullet}O_2^-$) species. Kinetic investigations revealed pseudo-first-order and Michaelis–Menten-type behaviour, while recyclability studies confirmed the structural integrity and reusability of the catalysts. Owing to its superior performance, ZnO-His was further employed for the UV-assisted hydrolysis of bioactive ester derivatives, such as ethyl gallate. The formation of the corresponding hydrolysis products was independently confirmed by ESI-MS analysis.

Received 16th February 2026
Accepted 16th May 2026

DOI: 10.1039/d6su00100a

rsc.li/rscsus



### Sustainability spotlight

This work presents a sustainable strategy for ester bond cleavage using low-temperature synthesized ZnO nanocatalysts, aqueous-phase catalysis, and light-assisted activation. The ZnO catalysts were synthesized *via* a facile co-precipitation method without toxic solvents or hazardous reagents, while moderate thermal treatment (300 °C) minimized energy consumption. Catalytic reactions were performed under mild aqueous conditions (pH 7.4), avoiding harsh chemicals and reducing waste generation. Histidine functionalization provided a biocompatible enzyme-mimetic catalytic interface without synthetic ligands. UV-assisted activation utilized the intrinsic semiconductor properties of ZnO, eliminating the need for external oxidants. The catalyst also exhibited good recyclability and stability, supporting resource efficiency and environmentally benign degradation of ester-based pollutants under green chemistry principles.

## 1. Introduction

Zinc oxide (ZnO) is a versatile, wide-band-gap semiconductor material that has attracted extensive attention in recent years owing to its unique physicochemical properties, including high thermal stability, tunable electronic structure, and strong redox potential. These attributes make ZnO an excellent candidate for diverse applications in photocatalysis, optoelectronics, environmental remediation, and sensor technology.[1] In particular, ZnO nanostructures have demonstrated remarkable catalytic activity in various organic transformations and pollutant degradation processes due to their high surface-to-volume ratio, abundance of surface defects, and rich oxygen-vacancy chemistry.[2] Among the diverse families of organic contaminants, ester and phosphoester-based species are of particular concern because of their ubiquity in agrochemicals, pharmaceuticals, and industrial effluents, as well as their persistence and ecotoxicity in aquatic environments.[3] Rational design of ZnO-based

[a]*Department of Chemistry, Birla Institute of Technology and Science Pilani, Hyderabad, India*

[b]*Materials Center for Sustainable Energy & Environment, Birla Institute of Technology and Science Pilani Hyderabad Campus, Hyderabad, 500078, India. E-mail: sounak.roy@hyderabad.bits-pilani.ac.in; nilanjan@hyderabad.bits-pilani.ac.in*

nanocatalysts that can efficiently promote ester bond cleavage under mild, aqueous conditions is therefore an important strategy for sustainable environmental remediation.[4]

The catalytic performance of ZnO is highly sensitive to its crystal size, surface area, and defect density, all of which are strongly influenced by synthesis parameters such as temperature, precursor concentration, and calcination conditions.[5] Among these, calcination temperature plays a decisive role in controlling the crystallinity, particle morphology, and surface hydroxylation of ZnO, which in turn dictate its catalytic efficiency.[6] Low-temperature calcination typically produces nanostructures with smaller crystallites, higher defect concentration, and abundant surface hydroxyl groups, whereas high-temperature calcination promotes particle growth and crystallinity, resulting in reduced surface area and lower reactivity. Therefore, precise thermal modulation serves as a key strategy to tune the surface and electronic properties of ZnO.[7] While structural control is essential, surface modification offers an additional dimension to tailor the chemical environment of active sites.[8] Functionalizing ZnO with organic ligands can alter its surface charge distribution, hydrophilicity, and catalytic selectivity. Among potential modifiers, histidine stands out due to its bifunctional coordination capability through imidazole and carboxylate groups. The anchoring of histidine onto ZnO surfaces can introduce Lewis acid-Bronsted base duality, stabilise surface defects, and facilitate proton transfer, collectively improving substrate adsorption and catalytic turnover.[9] Furthermore, the intrinsic photoresponsive behaviour of ZnO enables its activation under UV irradiation, where photon absorption excites electrons from the valence band to the conduction band, generating electron–hole ($e^-/h^+$) pairs. These photogenerated charge carriers migrate to the catalyst surface, initiating a cascade of redox processes.[10] The excited electrons reduce adsorbed oxygen molecules to form superoxide radicals ($^{\bullet}O_2^-$), while the holes oxidize surface hydroxyl groups or water molecules to produce highly reactive hydroxyl radicals ($^{\bullet}OH$).[11] These transient species act as powerful oxidants, driving the hydrolysis of organic substrates through a radical-mediated pathway. Thus, coupling surface modification with UV-induced photoactivation creates a synergistic enhancement of catalytic efficiency by facilitating charge separation, extending carrier lifetimes, and amplifying interfacial redox reactivity.[12]

In this study, ZnO nanocatalysts were synthesised *via* a co-precipitation route and thermally treated at different Calcination temperatures (300 and 700 °C) to investigate the influence of calcination on their physicochemical and catalytic properties. The catalytic performance of these materials was systematically evaluated through the hydrolysis of *p*-nitrophenyl acetate, its long-chain analogue at pH 7.4, enabling kinetic analysis of calcination-temperature effects, substrate structure dependence, catalyst loading and substrate concentration influences, Michaelis–Menten-type behaviour, *etc.* To further tailor the interfacial chemistry, ZnO-300 was functionalized with histidine through coordination-assisted modification, introducing Lewis acid-Bronsted base duality and enhanced hydrophilicity. While UV-light-driven studies, radical scavenger tests, and fluorescence probing of hydroxyl radicals elucidated the photoinduced charge-transfer and radical-mediated pathways that underpin the superior hydrolytic and photocatalytic activity of ZnO-300 and ZnO-Histidine under ambient and UV irradiation. Further, ZnO-Histidine has been utilized for efficient UV light-assisted hydrolysis of bioactive ester derivatives, such as ethyl gallate. The extent of hydrolysis in each case was interpedently assayed by ESL-MS.

## 2. Materials and methods

### 2.1 Synthesis

**2.1.1 Synthesis of ZnO-nanocatalyst (ZnO-*x*).** A Co-precipitation technique was employed to synthesize a series of ZnO Catalyst. In a typical procedure, zinc nitrate hexahydrate (99% AR grade) (0.5 g) was dissolved in deionized water (5 mL) under continuous stirring to obtain a clear solution in an air atmosphere. Separately, NaOH (AR grade, 98% pelletes)(0.10 g, 2.5 equiv. With respect to $Zn^{2+}$) was dissolved in a minimal amount of deionized water and then added slowly to the zinc nitrate solution under vigorous stirring. The resulting mixture was maintained at 60 °C and stirred for 3 h, leading to the formation of a white precipitate. The solid was collected by filtration, thoroughly washed several times with deionized water (~1000 mL) to remove residual ions, and dried in a hot-air oven to afford a white powder (0.250 g). The dried precursor was then calcined at different temperatures to obtain ZnO catalysts (ZnO-x) with distinct physicochemical properties. Calcination at 300 °C for 12 h yielded the ZnO-300 catalyst, while calcination at 700 °C for 12 h produced the ZnO-700 catalyst.[13]

**2.1.2 Synthesis of histidine-modified ZnO nanocatalyst (ZnO-His).** Dispersions of ZnO nanoparticles (2 mg $mL^{-1}$, 1 mL) were prepared in double-distilled water (DDW) and phosphate-buffered saline (PBS, 10 mM, pH 7.4) and added to L-histidine (AR grade 99% pure) solutions (1 mM, 1 mL). The resulting mixtures were maintained in a thermostated environment at 40 °C for 24 h to allow adsorption equilibrium between histidine molecules and the ZnO surface. After completion of the adsorption process, the samples were filtered to separate the solid ZnO nanoparticles from the supernatant. The recovered solids were thoroughly washed several times with deionized water to remove unbound histidine. Finally, the washed materials were dried in a hot-air oven to obtain the histidine-modified ZnO nanocatalyst, denoted as ZnO-His.[14]

### 2.2 Catalyst characterization

X-ray powder diffraction (XRD) was employed on the Rigaku Ultima IV X-ray diffractometer with Cu Kα radiation ($\lambda = 1.5418$ Å) at a scan rate of 1° $min^{-1}$ with a step size of 0.05°. The average nanocrystal diameters ($D$) were estimated using Scherrer's formula: $D = 0.9l/B\cos\theta$, where B is the full-width at half-maximum, $\lambda$ is the wavelength of the radiation, and $\theta$ is the corresponding angle. Nitrogen adsorption–desorption measurements were carried out at 77 K using a Microtrac BEL Corp mini II surface area and porosity analyser to determine the textural properties of the samples. Prior to analysis, the ZnO powders were degassed under vacuum at 200 °C for 2 hours to

remove physiosorbed species. The specific surface area was calculated from the adsorption branch of the isotherm using the Brunauer–Emmett–Teller (BET) model, while the pore size distribution and total pore volume were obtained from the desorption branch using the Barrett–Joyner–Halenda (BJH). Field-emission scanning electron microscopy (FESEM) was employed to examine the morphology and particle size of the ZnO samples. X-ray photoelectron spectroscopy (XPS) was performed to probe the chemical states of Zn and O in the samples using a Thermo Scientific K-Alpha surface-analysis spectrometer housing Al K$\alpha$ as the X-ray source (1486.6 eV). The binding energy scale was calibrated with reference to the C1s peak at 284.8 eV, and the data profiles were subjected to a nonlinear least–squares curve fitting program with a Gaussian–Lorentzian production function and processed with Avantage software. The solid-state UV spectra of the powdered samples were collected on a JASCO V-670 UV-visible spectrophotometer. The optical band gaps were estimated from the Kubelka–Munk transformed spectra by constructing Tauc plots of $(F(R)hv)^2$ *versus* $hv$ and extrapolating the linear region to the energy axis.

### 2.3 Catalytic test

A stock solution of *p*-nitrophenyl acetate (*p*-NPA, 0.50 mM) was first prepared in 5 mL PBS buffer solution (10 mM, pH 7.4). Subsequently, ZnO-*x* nanocatalyst (0.5 mg.mL$^{-1}$) was added to this solution, and the suspension was stirred at room temperature under ambient conditions. As the reaction proceeded, the solutions turned from turbid white to turbid yellow, indicating the formation of *para*-nitrophenolate ion (*p*-NP). At different time intervals, aliquots (2.0 mL) of the reaction mixture were withdrawn, and the solid catalyst was removed by centrifugation (16 000 rpm, 5 min). The clear supernatant was then analysed by UV-vis spectroscopy on a JASCO V-650 spectrophotometer to monitor the time-dependent evolution of the characteristic absorption band of *p*-nitrophenolate.

### 2.4 Scavenger experiments

A scavenger test was carried out using ZnO-*x* nanocatalyst during the hydrolysis of *p*-NPA to elucidate the roles of the key reactive species ($h^+$, $^{\cdot}OH$, and $^{\cdot}O_2^-$) in the catalytic process, respectively. In each experiment, 0.5 mg of ZnO-x nanocatalyst was taken in 5 mL of *p*-NPA (5 mM). A 2 mM solution of the individual radical scavenger was then added initially to the reaction mixture, followed by irradiation using a UV light with continuous stirring. The hydrolysis study was monitored every 5 minutes by measuring the absorbance value of the solution.

## 3. Results and discussion

### 3.1 Structural characterization of ZnO-x nanocatalyst

The textural properties of the ZnO nanoparticles calcined at different temperatures (300 and 700 °C), denoted as ZnO-300

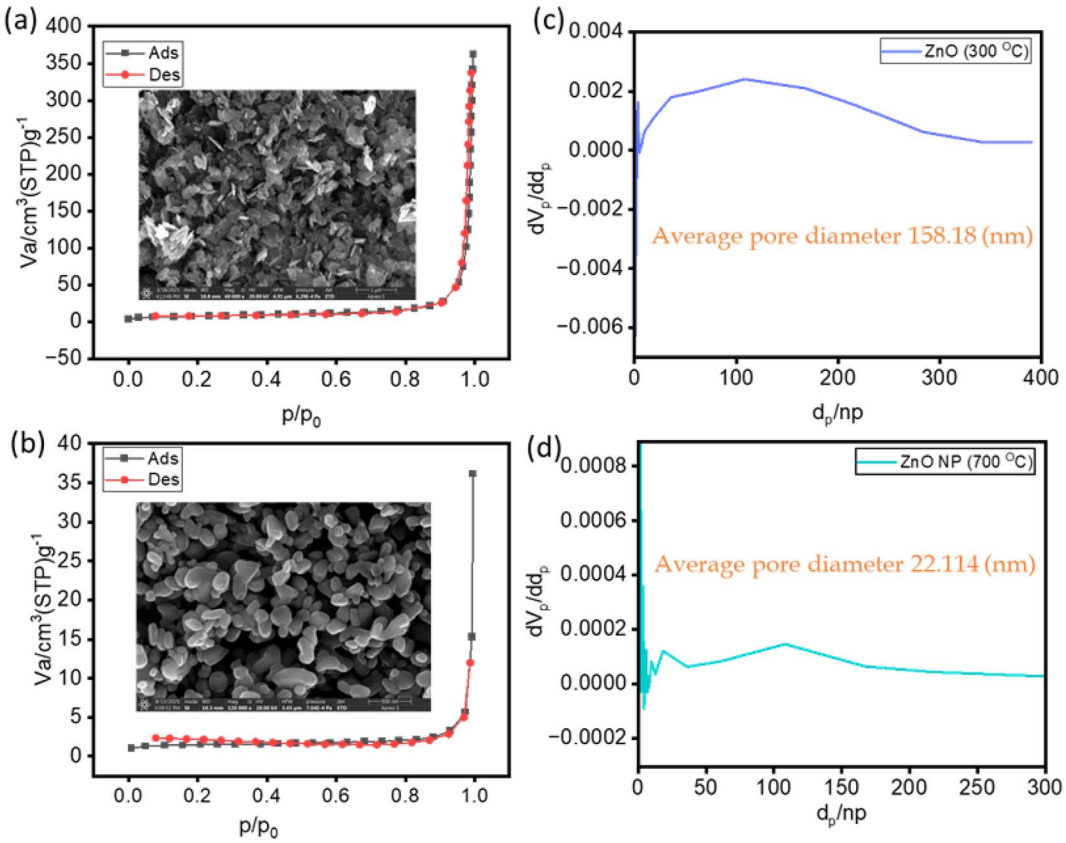


Fig. 1 BET adsorption isotherm of (a) ZnO-300 (nano flake), (b) ZnO-700 (polyhedron). Average pore size of (c) ZnO-300 and (d) ZnO-700 nanoparticle.

and ZnO-700, were investigated by $N_2$ adsorption–desorption measurements. As shown in Fig. 1, both samples exhibit type-II adsorption isotherms according to the IUPAC classification, which is typically associated with non-porous or macroporous solids where nitrogen adsorption occurs predominantly on the external surfaces of the particles.[15] The overall shape of the isotherms suggests monolayer adsorption at low relative pressures followed by multilayer adsorption at higher pressures, indicating the absence of well-defined intrinsic mesoporosity within the ZnO framework. The Brunauer–Emmett–Teller (BET) analysis indicated that ZnO-300 exhibits a considerably higher specific surface area (25.8 $m^2\ g^{-1}$) compared to ZnO-700 (5.4 $m^2g^{-1}$), indicating that increasing the calcination temperature leads to a pronounced reduction in accessible surface area (Fig. 1a and b). This decrease can be attributed to thermally induced particle growth and sintering during high-temperature calcination, which reduces the external surface area by promoting agglomeration and partial coalescence of ZnO nanoparticles.[16] In addition, the ZnO-300 (Fig. 1c) exhibited a larger average pore diameter (158.1 nm) compared to ZnO-700 (22.1 nm), suggesting that low-temperature calcination preserves a more open texture (Fig. 1d). Upon calcination at 700 °C, enhanced densification and structural rearrangement lead to more compact particle assemblies, resulting in smaller interparticle voids and a corresponding decrease in surface area.[17] The observed pore size distribution in both ZnO-300 and ZnO-700 primarily arises from interparticle voids rather than intrinsic porosity. The larger apparent pore diameter in ZnO-300 reflects the loosely packed nanoflake morphology, leading to significant macroporous void spaces. In contrast, the reduced pore diameter in ZnO-700 originates from densification and particle growth at higher calcination temperature, resulting in smaller interparticle gaps.

Subsequently, the crystalline structure and phase purity of ZnO-300 and ZnO-700 were examined by powder X-ray diffraction (PXRD) to correlate the observed textural properties with their crystal framework. Fig. 2a showed the diffraction patterns of ZnO-300 confirm complete conversion of the precursor to crystalline ZnO nanostructures, with the main reflections at $2\theta$ = 31.8°, 34.4°, and 36.3° indexed to the (100), (002), and (101) planes of hexagonal wurtzite ZnO (space group $P6_3mc$).[18] The absence of additional diffraction peaks indicates the high phase purity of both samples. Notably, ZnO-700 exhibits significantly sharper and more intense diffraction peaks than ZnO-300, indicating enhanced crystallinity as a result of high-temperature calcination (Fig. 2b). In contrast, the broader and less intense peaks of ZnO-300 indicate a smaller crystallite size, increased lattice strain, and a higher density of structural defects.

As illustrated in Scheme 2, calcination of the Zinc nitrate hexahydrate (Zn–NH) precursor for an identical duration (6 h) at different temperatures (300 and 700 °C) induces pronounced morphological evolution of the resulting ZnO nanostructures. A field-emission scanning electron microscope (FESEM) has been utilised to analyse the morphology of ZnO samples. The FESEM image of ZnO-300 clearly shows the formation of a 3D nanoflake at 300 °C. Upon increasing the temperature to 700 °C, the 3D nanoflake breaks to form a 3D polyhedron.[19] The EDAX mapping in Fig. S1 confirmed the high distribution of Zn and O in the matrix.

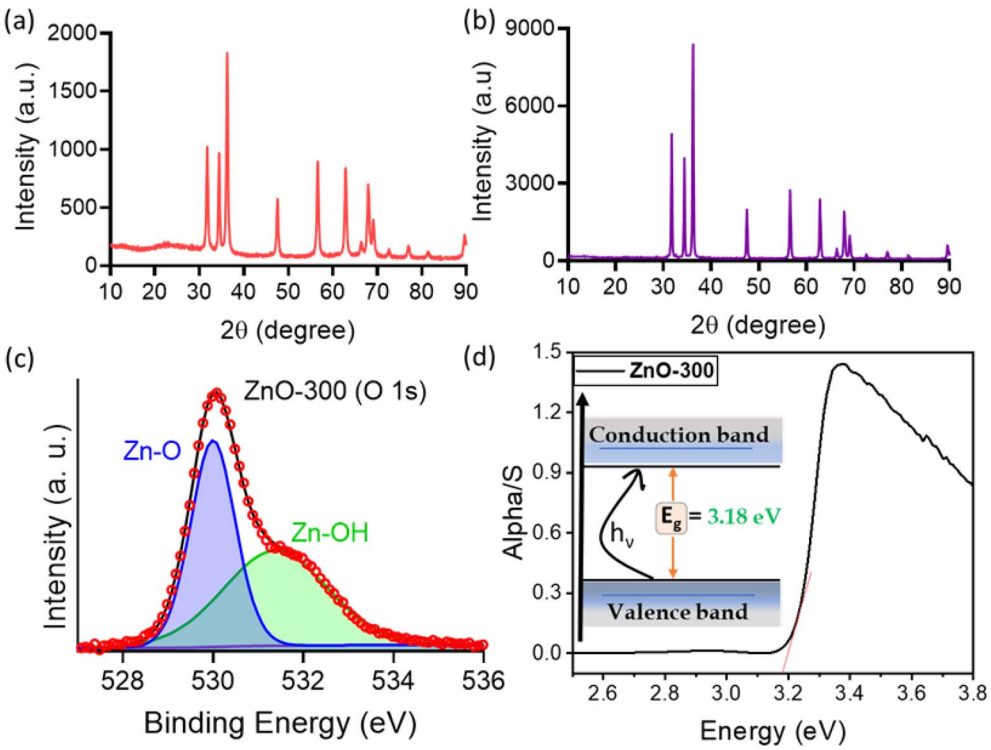


Fig. 2 PXRD patterns of (a) ZnO-300, (b) ZnO-700. (c) O 1s core level XPS spectrum of ZnO-300 (d) Band gap elucidation of ZnO-300.

### 3.2 Surface and electronic characterization of ZnO-*x* nanocatalysts

In addition to structural and morphological characterisation, the optical properties of ZnO-300 and ZnO-700 were investigated using UV-Vis diffuse reflectance spectroscopy (UV-Vis DRS). ZnO, being a direct wide-band-gap semiconductor, exhibited characteristic absorption edges in the UV region.[20] As shown in Fig. S2, ZnO-300 exhibits absorbance maxima at 367 nm, while ZnO-700 shows a slightly red-shifted maxima at 370 nm. This shift toward longer wavelength suggests a minor decrease in the optical band gap with increasing calcination temperature.[21] Correspondingly, the calculated band gap values were found to be 3.18 eV for ZnO-300 (Fig. 2d) and 3.16 eV for ZnO-700 (Fig. S3). The slight reduction in band gap energy at higher temperature can be attributed to the increase in crystallite size and reduction of quantum confinement effects as the nanoparticles grow larger during calcination. At lower temperature (300 °C), ZnO nanoparticles possess smaller crystallites and higher concentrations of surface defects such as oxygen vacancies and zinc interstitials, which introduce localised states near the conduction and valence bands and enhance quantum confinement effects, leading to a slightly wider band gap. With increased calcination temperature (700 °C), the enhanced crystallinity and reduced lattice strain promote better overlap between Zn 4S and O 2p orbitals, narrowing the separation between the valence band maximum and the conduction band minimum. This structural and electronic reorganisation facilitates lower-energy electronic transitions, consistent with the observed red shift in the optical absorption spectrum.[22] Additionally, Raman spectroscopy was employed to further confirm the structural quality of the synthesized ZnO samples. As shown in Fig. S12, both ZnO-300 and ZnO-700 exhibit the characteristic Raman active modes of hexagonal wurtzite ZnO. The strong peak observed around at 436 $cm^{-1}$ corresponds to the $E_2$ (high) mode, which is associated with the vibration of oxygen atoms in the ZnO lattice and confirms the high crystallinity of the samples. The peak at 328 $cm^{-1}$ is attributed to the second-order Raman processes, and 378 $cm^{-1}$ corresponds to A1 (TO).

To further correlate the optical behaviour with the surface chemical composition and electronic structure, X-ray photoelectron spectroscopy (XPS) analysis was performed for ZnO-300 and ZnO-700 samples. Both samples exhibited a characteristic Zn $2p_{3/2}$ peak centred at approximately 1021.5 eV, confirming the presence of $Zn^{2+}$ species in the wurtzite ZnO lattice (Fig. S4).[23] The corresponding O 1 s spectra of the samples show two distinct deconvoluted peaks. The dominant low-binding-energy peak, located at 529.9 eV and 530.5 eV for ZnO-300 (Fig. 2c) and ZnO-700 (Fig. S5), respectively, corresponds to lattice oxygen ($O^{2-}$) bound to $Zn^{2+}$ within the ZnO crystal structure. The higher-binding-energy component, appearing at 531.5 eV and 532.2 eV for ZnO-300 and ZnO-700, respectively, is attributed to surface-adsorbed hydroxyl groups (–OH).[24] The relative area of the O–H component is found to be higher for ZnO-300 (52%) compared to ZnO-700 (44%), indicating that the lower temperature sample possesses a greater concentration of surface-adsorbed oxygen and hydroxyl groups. This can be correlated with the higher surface defect density and larger specific surface area of ZnO-300, which provides more active sites for adsorption. In contrast, the reduction in O–H contribution for ZnO-700 suggests enhanced crystallinity and surface densification at elevated calcination temperature, leading to fewer surface defects and reduced hydroxyl adsorption.

### 3.3 Hydrolysis of acyl esters by ZnO nanocatalyst

**3.3.1 Effect of ZnO calcination temperature on catalytic activity.** In light of the contrasting structural, optical, and surface properties of ZnO nanomaterials, their influence on catalytic activity was further investigated through the hydrolysis of ester substrate. For this study, *p*-nitrophenyl acetate (PNPA, 0.5 mM) was employed as a model substrate to evaluate the catalytic efficiency of the ZnO-300 (3D nanoflake, 0.5 mg $mL^{-1}$) sample under natural daylight conditions at PBS buffer (pH 7.4). The progress of the reaction was monitored by UV-vis spectroscopy, recording spectra at 5 min intervals over a period of 50 min (Fig. 3a). A gradual increase in the absorption intensity near 400 nm was observed with time, corresponding to the formation of *p*-nitrophenolate ion (p-NP), the hydrolysis product of PNPA.[25] The kinetic analysis of the absorbance-time data revealed that the reaction followed pseudo-first-order kinetics with an apparent rate constant ($k$) of 0.0080 $min^{-1}$, demonstrating the efficient catalytic behaviour of the ZnO-300 nanoflake under ambient illumination (Fig. 3b).

In contrast, the ZnO-700 (3D polyhedron) catalyst exhibited a noticeably slower reaction rate, with a reduced apparent rate constant of 0.0048 $min^{-1}$ (Fig. S6). The decrease in reaction rate for ZnO-700 can be attributed to its larger crystallite size, lower surface area, and diminished concentration of surface hydroxyl groups, as evidenced by the XPS analysis. The abundant surface –OH groups and higher defect density in ZnO-300 facilitate efficient adsorption and activation of water and substrate molecules, promoting rapid hydrolysis of the ester. In contrast, the improved crystallinity and reduced surface defect density of ZnO-700 limit the availability of active surface sites, leading to slower catalytic conversion.[26] To enable a more rigorous comparison of catalytic performance, the pseudo-first-order rate constants were further normalized with respect to catalyst mass and BET surface area. The mass-normalized rate constants ($k_m$) retain the original trend, with ZnO-300 exhibiting higher activity than ZnO-700 (Table S1). However, ZnO-700 demonstrates higher catalytic activity per unit surface area, upon normalization by surface area ($k_s$). This indicates that the enhanced apparent activity of ZnO-300 primarily arises from its larger specific surface area, which provides a greater number of accessible active sites. In contrast, ZnO-700 exhibits higher intrinsic catalytic efficiency per unit surface area.[27] These results highlight the importance of distinguishing between surface–area–driven activity and intrinsic catalytic performance in heterogeneous catalytic systems.

**3.3.2 Steric influence of substrate chain length on hydrolysis.** To further probe the influence of substrate structure on catalytic efficiency, *p*-nitrododecanoate (PNPD) was introduced as a long-chain analogue of PNPA. Long-chain esters like PNPD

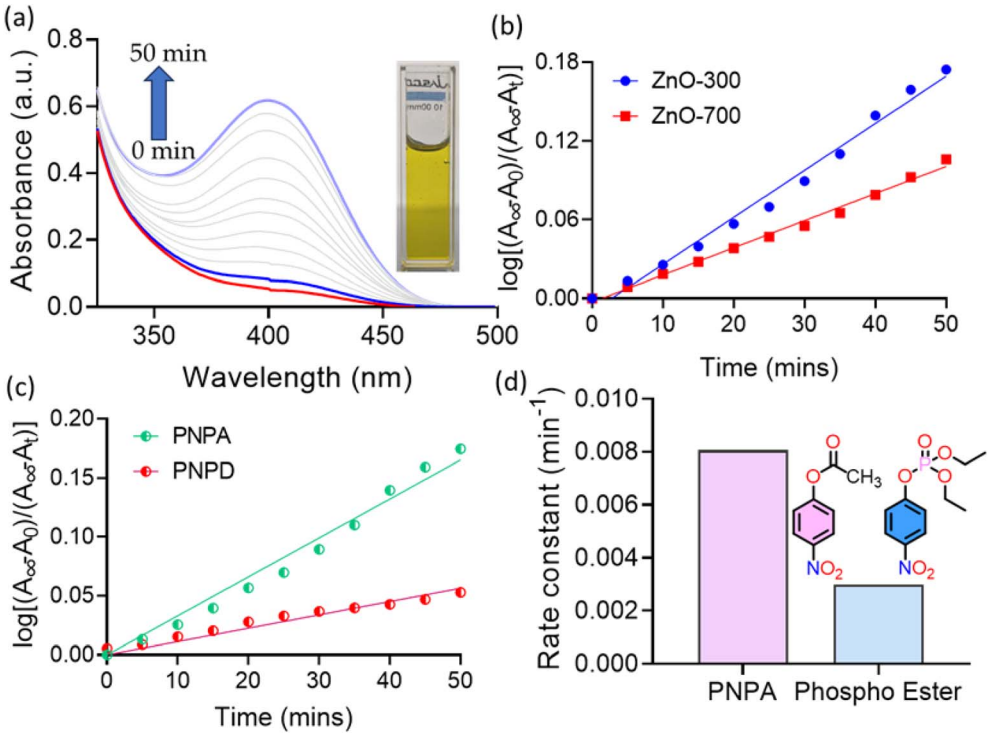


Fig. 3 (a)Time-dependent changes in UV-visible spectra of PNPA (0.5 mM) in the presence of ZnO-300 (0.5 mg $mL^{-1}$) at pH 7.4 in buffered medium. (b) Kinetic plots comparing ZnO-300 and ZnO-700 on the catalytic hydrolysis of PNPA in pH 7.4. (c) Kinetic plots on the catalytic hydrolysis of PNPA *vs.* PNPD in pH 7.4, in the presence of ZnO-300. (d) Determination of pseudo-first-order rate constant comparing PNPA *vs.* phosphoester.

are environmentally significant due to their hydrophobic nature, low biodegradability, and potential ecotoxicity, which lead to persistence and accumulation in aquatic systems.[28] Understanding their catalytic degradation is therefore crucial for developing efficient ZnO-based materials for environmental remediation. Kinetic analysis of the hydrolysis of PNPD revealed that the reaction proceeded with a pseudo-first-order rate constant of 0.0020 $min^{-1}$, under identical reaction conditions, confirming that ZnO-300 is capable of catalysing the cleavage of the more hydrophobic ester. However, the rate was approximately 4-fold lower than that observed for PNPA ($k$ = 0.0080 $min^{-1}$), indicating that substrate structure significantly influences catalytic efficiency (Fig. 3c). The reduced reactivity of PNPD can be attributed to its longer aliphatic chain, which increases hydrophobicity and introduces steric hindrance around the carbonyl group and restricts its accessibility to the Lewis acidic $Zn^{2+}$ active sites. Moreover, the nonpolar chain limits solubility, diffusion and water adsorption near the catalytic interface, diminishing the probability of nucleophilic attack. As a result, despite the $Zn^{2+}$ centres remaining catalytically active, the combined effects of steric hindrance, poor solubility, and hydrophobic shielding significantly lower the hydrolysis rate of PNPD compared to PNPA.[29]

To further explore the substrate-dependent nature of ZnO-mediated catalysis, we investigated the phospho ester, which features P–O bonds with distinct electronic and steric environments compared to C–O esters. Phosphoesters are environmentally relevant analogues due to their occurrence in organophosphorus pollutants and biomolecules, and their hydrolysis behaviour can provide deeper insight into catalytic versatility of ZnO. A pseudo-first-order rate constant of 0.0030 $min^{-1}$ was obtained for phosphoester hydrolysis, suggesting that ZnO-300 facilitates bond cleavage through a mechanism that remains effective even when the reactive centre shifts from carbonyl to phosphoryl (Fig. 3d). Interestingly, this rate constant lies between those obtained for PNPA (0.0080 $min^{-1}$) and PNPD (0.0020 $min^{-1}$), indicating that the reactivity of the phosphoester is governed by a balance between electronic and structural effects. The moderately enhanced rate compared to PNPD can be attributed to the higher polarity of the phosphoester, which promotes better adsorption and interaction with the hydrophilic ZnO surface, facilitating nucleophilic attack by surface hydroxyl groups.[30] However, the rate remains lower than that of PNPA, reflecting the intrinsic strength and stability of the P–O bond relative to the C–O bond, as well as the reduced electrophilicity of the phosphorus centre. These observations highlight that while ZnO-300 retains catalytic activity toward diverse ester types, substrate structure-particularly bond nature, polarity, and steric environment-plays a decisive role in determining hydrolysis efficiency.[31]

**3.3.3 Influence of catalyst loading and substrate concentration.** Systematic kinetic experiments were conducted by varying both catalyst loading and substrate concentration under identical conditions. As shown in Fig. 4a, increasing the ZnO-

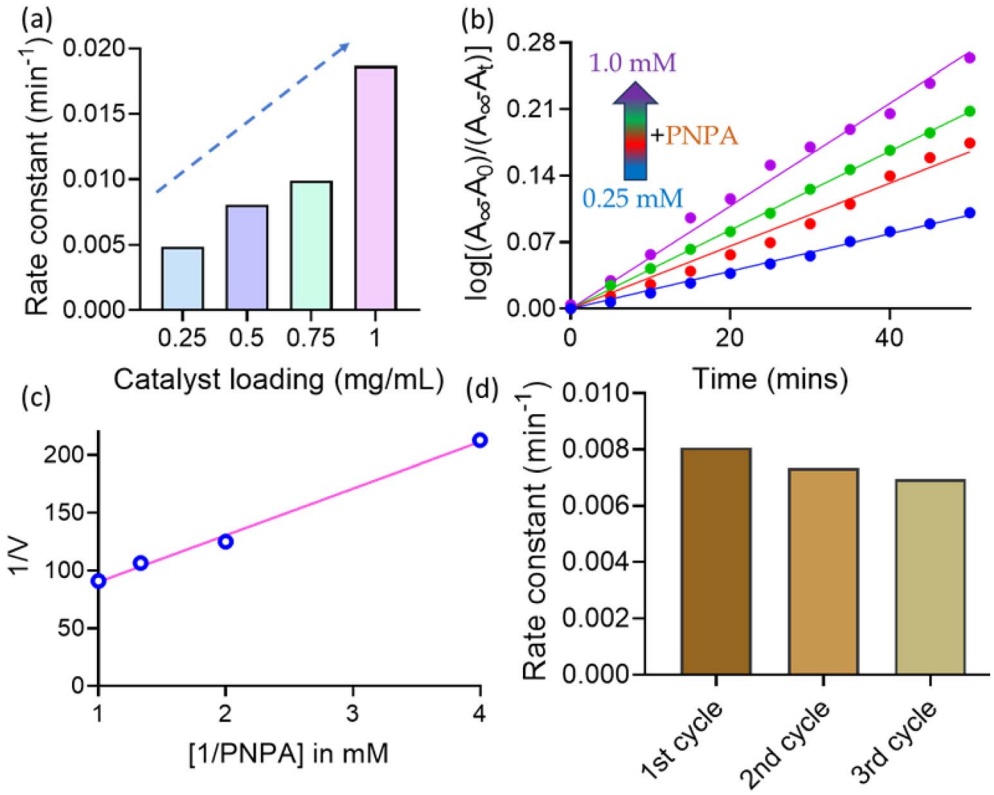


Fig. 4 (a) Effect of concentration of ZnO-300 on catalytic hydrolysis of PNPA (0.5 mM) at pH 7.4. (b) Effect of concentration of PNPA on catalytic hydrolysis by ZnO-300 (0.5 mg $mL^{-1}$) at pH 7.4. (c) Lineweaver–Burk plot of PNPA hydrolysis catalysed by ZnO-300 in pH 7.4. (d) Cycle study of ZnO-300 of PNPA hydrolysis in pH 7.4.

300 concentration from 0.25 to 1.0 mg. $mL^{-1}$ led to a corresponding rise in the pseudo-first-order rate constant ($k$) from 0.0048 to 0.018 $min^{-1}$, respectively. This pronounced enhancement in rate constant ($k$) can be attributed to the greater number of accessible active sites provided by the higher mass of ZnO-300, which increases the available surface area and density of surface $Zn^{2+}$ or Zn–OH groups responsible for ester adsorption and activation. As the catalyst concentration increases, PNPA molecules experience more frequent and effective collisions with the ZnO surface, thereby reducing competition for adsorption sites and facilitating more efficient interfacial nucleophilic attack on the ester bond.[32] On the other hand, when the substrate concentration was varied from 0.25 mM to 1.0 mM under identical reaction conditions, the rate constant increased from 0.0047 $min^{-1}$ to 0.011 $min^{-1}$ (Fig. 4b). The gradual enhancement in rate with increasing PNPA concentration indicates that the reaction follows pseudo-first-order kinetics with respect to the substrate at lower concentrations.[33] This trend can be attributed to the increased frequency of productive encounters between PNPA molecules and catalytically active ZnO-300 surface sites as substrate concentration rises, which enhances adsorption and promotes the efficient formation of the activated ester-ZnO interfacial complex necessary for nucleophilic attack and bond cleavage.[34]

Since the rate of the hydrolysis reaction was linearly dependent on the substrate concentration when the substrate concentration was low, it suggests Michaelis–Menten-type kinetics. Thus, to better understand the kinetics, a Lineweaver–Burk plot is constructed by plotting the reciprocal of the initial reaction rate ($1/V$) against the reciprocal of the substrate concentration ($1/[S]$). The linearised form of the Michaelis–Menten equation is given by:

$$\frac{1}{v} = \frac{k_m}{v_{max}[S]} + \frac{1}{v_{max}} \quad (1)$$

where $V$ and $V_{max}$ are the initial hydrolysis rate and the maximum hydrolysis rate, $K_m$ is the Michaelis constant, and $[S]$ is the substrate concentration. Thus, the dependence of $1/V$ and $1/[S]$ is shown in Fig. 4c, it can be seen that $1/V$ is linear to $1/[S]$. From the linear fit, the kinetic parameters were obtained as $K_m$ = 0.82 mM and $V_{max}$ = 0.020 mM $min^{-1}$.[35]

**3.3.4 Thermally induced modulation of catalytic activity.** Temperature is a critical factor governing both the kinetics and thermodynamics of catalytic reactions, as it affects molecular motion, collision frequency, and activation energy.[36] To assess this, the hydrolysis of PNPA was carried out at different temperatures ranging from 25 °C to 35 °C under identical reaction conditions, and the corresponding pseudo-first-order rate constants were determined (Fig. 5a). An increase in reaction rate from 0.0080 $min^{-1}$ to 0.012 $min^{-1}$ with temperature was observed, consistent with the Arrhenius behaviour of thermally activated processes.

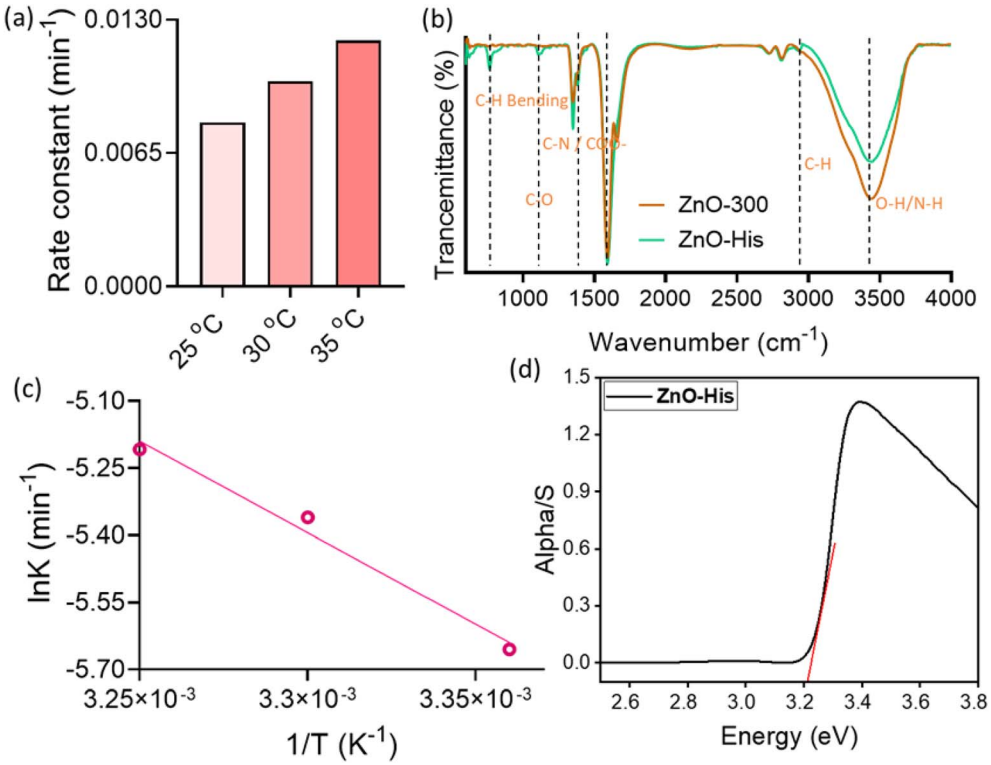


Fig. 5 (a) Rate of hydrolysis of PNPA (0.5 mM) at different temperatures in the presence of ZnO-300 (0.5 mg $mL^{-1}$) at pH 7.4. (b) FT-IR spectra of ZnO-300 and ZnO-histidine (c) determination of activation energy (d) band gap elucidation of ZnO-Histidine.

$$K = Ae^{-\frac{E_a}{RT}} \quad (2)$$

where $k$ is the rate constant, $A$ is the pre-exponential factor, $E_a$ is the activation energy, $R$ is the universal gas constant, and $T$ is the absolute temperature (in Kelvin). At lower temperatures ($k$ = 0.0080 $min^{-1}$), the reaction proceeds more slowly due to reduced molecular motion and a lower fraction of reactant molecules possessing sufficient energy to overcome the activation barrier (Ea = 33.64 kJ $mol^{-1}$). As the temperature increases ($k$ = 0.012 $min^{-1}$), the enhanced thermal energy accelerates diffusion of PNPA toward the ZnO surface, increases the frequency of productive encounters with surface hydroxyl sites, and facilitates more efficient formation of the activated ester–ZnO complex, thereby promoting faster nucleophilic attack and bond cleavage.[37] This temperature-dependent enhancement confirms that the reaction is kinetically controlled within the studied range and follows classical Arrhenius behaviour (Fig. 5c).

**3.3.5 Catalyst recyclability and structural robustness.** The long-term stability and reusability of ZnO-300 were evaluated through consecutive hydrolysis cycles of PNPA under identical reaction conditions to assess its catalytic durability (Fig. 4d). After the 3rd consecutive cycle, the rate constant decreases approximately 11%. The gradual reduction in activity over successive runs suggests minor deactivation of the catalyst surface, possibly due to partial surface coverage by adsorbed reaction products, such as p-NP species, which can block active $Zn^{2+}$ and surface hydroxyl sites.[38] However, the relatively small decline in rate indicates that the ZnO-300 catalyst retains most of its activity even after multiple cycles, demonstrating good structural robustness and chemical stability under hydrolytic conditions. The slight loss in performance may also arise from partial loss of surface –OH groups during recovery and washing steps.[39] Nevertheless, the consistent catalytic behaviour across repeated uses confirms that ZnO-300 is a recyclable and durable catalyst, suitable for extended application in environmental remediation processes.

**3.3.6 Coordination-assisted surface modification of ZnO-300 by histidine.** To modulate the surface chemistry and active-site environment of ZnO-300 for enhanced catalytic performance, surface modification through coordination-assisted functionalization was undertaken. Surface modification is a powerful strategy to tune the physicochemical and electronic properties of metal oxide catalysts by introducing organic or inorganic ligands that can modulate surface charge distribution, hydrophilicity, and active-site accessibility. Such modifications can also improve substrate adsorption, suppress particle aggregation, and enhance catalytic efficiency. Among various potential modifiers, histidine was selected due to its unique bifunctional coordination capability. The imidazole and carboxylate groups of histidine can strongly coordinate with surface $Zn^{2+}$ centers, forming stable Zn–N and Zn–O bonds, while its amino functionality introduces additional hydrogen-bonding and acid–base interaction sites. These features are expected to stabilise the surface structure, increase the density of reactive sites, and facilitate substrate activation during hydrolysis.[40]

**3.3.7 Structural and electronic characterisation of ZnO-300-histidine.** The successful anchoring of histidine onto the ZnO-300 surface was confirmed through FTIR, XPS, and UV-Vis analyses, revealing characteristic bands corresponding to coordinated imidazole and carboxylate groups, indicative of strong ligand–surface interactions. The FTIR spectrum of native ZnO (Fig. 5b) displays a characteristic broad absorption band centred around 3445 $cm^{-1}$ corresponds to the O–H stretching vibrations of surface hydroxyl groups and adsorbed water molecules.[41] However, in ZnO-His, this band becomes broader and slightly shifts toward lower wavenumbers (3434 $cm^{-1}$), reflecting additional N–H and O–H stretching contributions from histidine molecules hydrogen-bonded or coordinated to surface $Zn^{2+}$ sites. Distinct new absorptions appear near 1387 $cm^{-1}$, which can be attributed to C–N and symmetric -$COO^{-}$ stretching vibrations, confirming the presence of histidine functionalities on the surface. In addition, the appearance of bands at 1110 $cm^{-1}$ and 760 $cm^{-1}$, corresponding to C–O stretching and C–H bending modes, respectively, further supports the successful anchoring of histidine onto the ZnO framework. The XRD pattern of ZnO-His retained all the characteristic diffraction peaks of wurtzite ZnO, confirming that the bulk crystalline structure remained intact after surface modification (Fig. S7). However, the peaks became slightly broader compared to pristine ZnO-300, indicating a minor reduction in crystallite size and increased surface disorder arising from the coordination of histidine molecules onto the ZnO surface.[42] This broadening reflects surface functionalization without any alteration to the intrinsic lattice framework. Further morphological analyses provide additional support for successful histidine functionalization. FESEM image reveals that both ZnO-300 and ZnO-His retain their nanoscale morphology with uniformly distributed particles, though the ZnO–His surface appears slightly roughened, consistent with organic layer deposition (Fig. 6c). EDAX mapping confirms the presence of C and N elements in ZnO-His, validating histidine incorporation without altering the overall stoichiometry (Fig. 6d). Moreover, zeta potential measurements show a shift toward more positive values upon histidine modification, reflecting the introduction of protonated amine groups and increased surface charge density (Fig. 6a). Native ZnO-300 exhibited a zeta potential of −35.0 mV, while free histidine showed −9.18 mV after surface coordination, ZnO-His displayed an intermediate value of −17.74 mV. This shift confirms partial neutralisation of surface hydroxyl charges by histidine.[43]

To further elucidate the surface chemical environment and elemental interactions induced by histidine modification, X-ray photoelectron spectroscopy (XPS) analysis was conducted. The XPS spectrum of ZnO-His exhibits a characteristic Zn $2p_{3/2}$ peak at 1021.5 eV, confirming the presence of $Zn^{2+}$ in the wurtzite ZnO lattice (Fig. S8). The appearance of an additional N 1s signal at 406 eV verifies the successful incorporation of histidine onto the ZnO surface. The O 1s spectrum shows two deconvoluted peaks at 530.48 eV and 532.23 eV, corresponding to lattice oxygen and surface hydroxyl groups, respectively (Fig. 6b). The slight shift of the surface adsorbed –OH peak

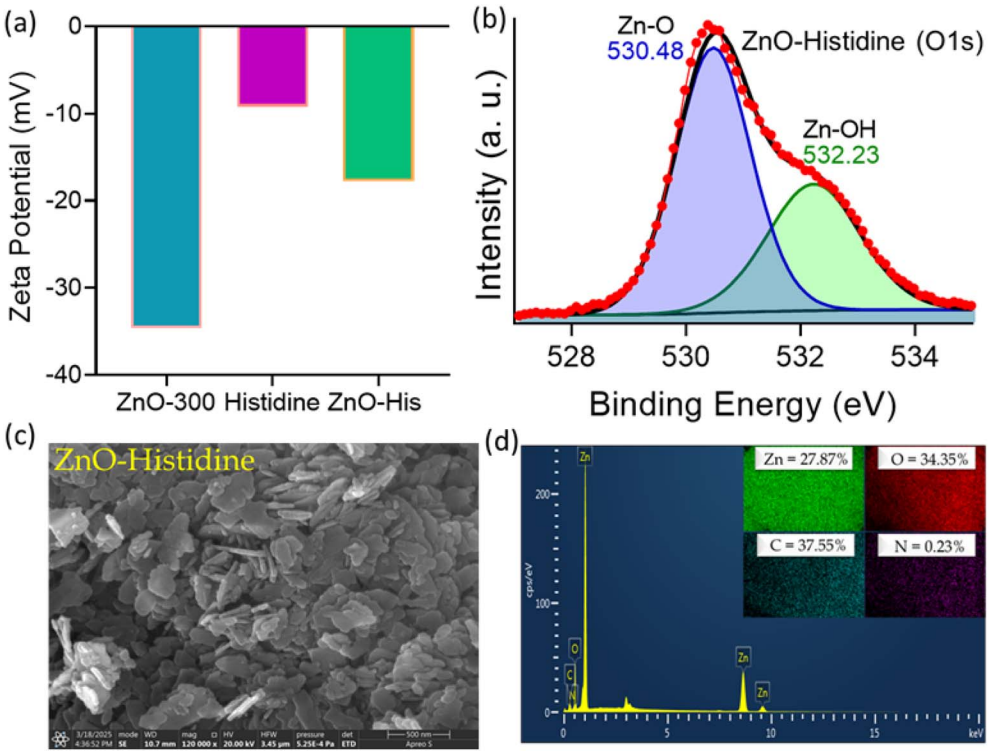


Fig. 6 (a) Zeta potential value of ZnO-300, Histidine and ZnO-Histidine in pH 7.4. (b) O 1s core level XPS spectrum of ZnO-Histidine. (c) FESEM image of ZnO-Histidine. (d) EDAX mapping of ZnO-histidine.

toward higher binding energy relative to ZnO-300 indicates a more electron-deficient oxygen environment, which can be rationalised by coordination of histidine to surface $Zn^{2+}$ centres and the resulting modification of local electron density and hydrogen-bonding environment at the hydroxyl sites.[44] A slight increase in the optical band gap (3.22 eV) was observed after histidine modification, as evident from the UV-Vis absorption analysis (Fig. 5d). The marginal blue shift in the absorption maxima suggests passivation of surface defect states due to histidine coordination. Altogether, these observations demonstrate that ZnO-His surface modification was successfully achieved while preserving the native crystalline structure of ZnO.[45]

**3.3.8 Synergistic enhancement in catalytic activity *via* histidine functionalization.** The catalytic hydrolysis of PNPA was further examined using a histidine-functionalized ZnO nanocatalyst (ZnO-His) to evaluate the effect of surface coordination on catalytic efficiency. The reaction was carried out under identical reaction conditions for a total duration of 50 minutes, with UV-vis spectra recorded at 5 minutes intervals to monitor the progressive hydrolysis of PNPA. Fig. 7a clearly illustrates that the rate constant increased to 0.012 $min^{-1}$ in the presence of ZnO–His, compared to pristine ZnO-300 ($k$ = 0.0080 $min^{-1}$), demonstrating the enhanced catalytic efficiency imparted by histidine functionalization. The carboxylate ($-COO^-$) and amine ($-NH_2$) groups of histidine coordinate with surface $Zn^{2+}$ centres through stable Zn–O and Zn–N bonds, subtly altering the surface electronic environment while preserving the wurtzite structure.[46] This coordination increases surface hydrophilicity, promoting more efficient adsorption and diffusion of water and substrate molecules near the active sites. Simultaneously, the imidazole moiety of histidine plays a crucial catalytic role through its proton-shuttling and base-assisting behaviour.[47] The imidazole nitrogen acts as a general base, abstracting protons from water or surface –OH groups to form reactive $-OH^-$ species, which attack the polarised carbonyl carbon of PNPA, which is already electronically destabilised through coordination to Lewis-acidic $Zn^{2+}$ centres. The dual functionality of $Zn^{2+}$ (as a Lewis acid) and histidine (as a Brønsted base) thus creates a bifunctional catalytic interface, promoting efficient substrate polarisation, transition-state stabilisation, and rapid bond cleavage, which accounts for the significantly improved catalytic performance of ZnO-His compared to unmodified ZnO-300.

**3.3.9 Photo-induced catalytic activation of ZnO-based nanocatalysts.** To further explore the light-responsive catalytic behaviour of ZnO-based materials, the study was extended to evaluate their performance under UV illumination. Upon UV illumination, both ZnO-300 and ZnO-His exhibited a pronounced enhancement in catalytic activity toward PNPA hydrolysis, highlighting the photoresponsive nature of these nanocatalysts (Scheme 1). The reaction rate for ZnO-300 increased significantly under UV exposure ($k$ = 0.015 $min^{-1}$) compared to daylight conditions ($k$ = 0.0080 $min^{-1}$) (Fig. 7b), while ZnO-His exhibited an even greater enhancement ($k$ =

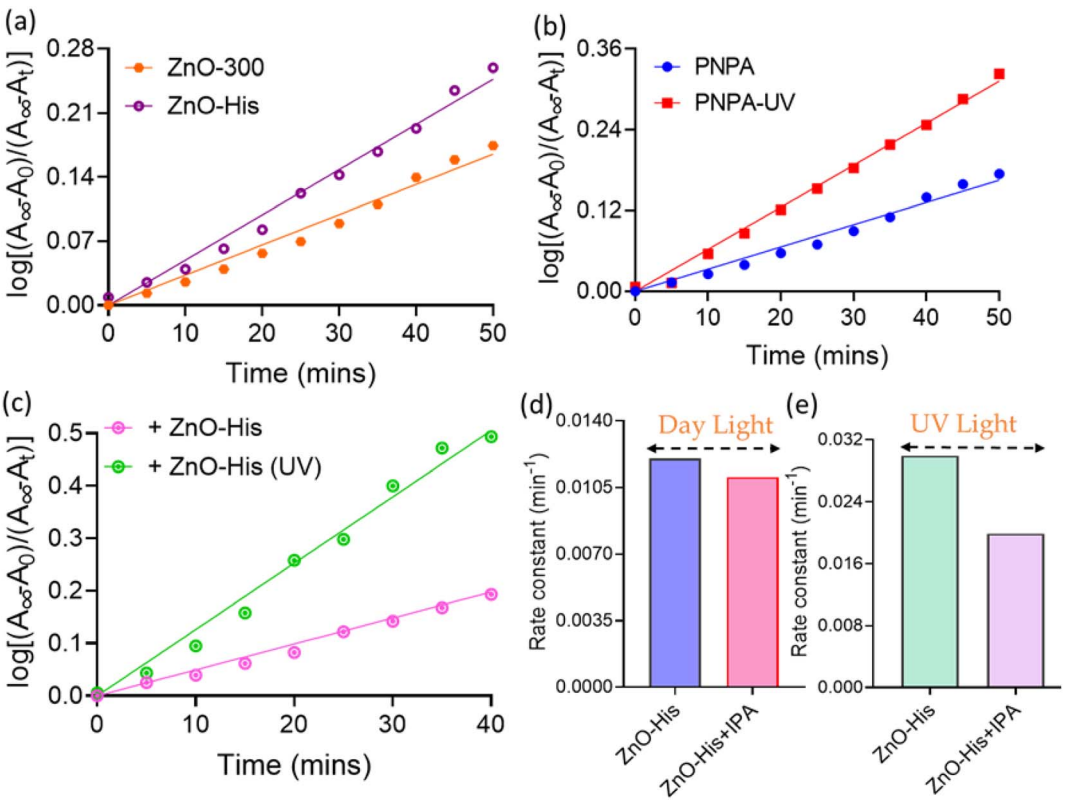


Fig. 7 (a) Determination of pseudo-first-order rate constant on catalytic hydrolysis of PNPA in the presence of ZnO-300 and ZnO-Histidine. Comparison of pseudo-first-order kinetic plots for PNPA hydrolysis under daylight and UV irradiation (b) in the presence of ZnO-300. (c) In the presence of ZnO-Histidine. (d) In daylight (e) in UV-light irradiation.

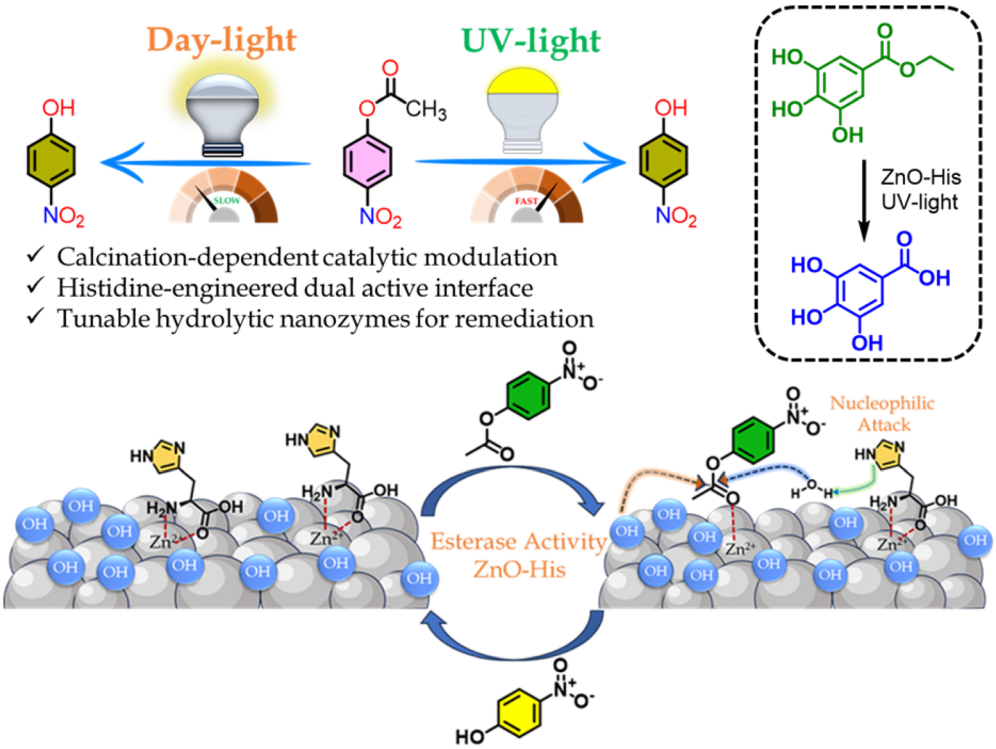


Scheme 1 Schematic illustration of calcination-dependent esterase–mimetic activity and UV-assisted diacylation by histidine-functionalized ZnO nanostructures and application to hydrolysis of bioactive esters, such as ethyl gallate.

0.029 $min^{-1}$) relative to its daylight performance ($k$ = 0.012 $min^{-1}$) under identical conditions (Fig. 7c). Control experiments were conducted under identical conditions in the absence of catalyst. As shown in Fig. S11a, the time-dependent UV-vis spectra of PNPA under UV irradiation without a catalyst exhibit only a minimal increase in absorbance over 50 min, indicating negligible direct photolysis. The corresponding pseudo-first-order kinetic plot affords a very low rate constant ($k$ = 0.0012 $min^{-1}$), which is significantly lower than that observed in the presence of ZnO-based catalysts. This enhancement can be attributed to the photoexcitation of ZnO, where UV photons excite electrons from the valence band to the conduction band, generating electron–hole ($e^-/h^+$) pairs that initiate surface redox reactions and enhance catalytic activity. Photogenerated holes oxidise surface hydroxyls or water molecules to produce reactive $^{\bullet}OH$ species.[48] To substantiate the involvement of photo-

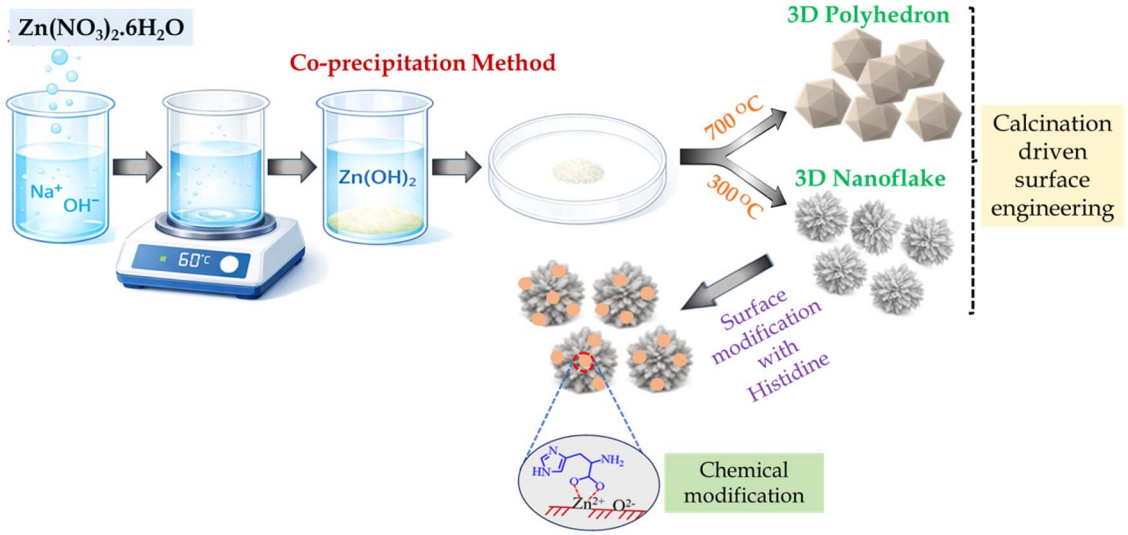


Scheme 2 Schematic illustration of the synthesis process ZnO nanostructures (a) surface engineering by modulating calcination temperature (b) chemical modification by histidine functionalization.

generated reactive species, a free radical capture experiment was performed using terephthalic acid (TA) as a fluorescence probe (Fig. S9). Native TA displayed an emission maximum at 350 nm, whereas in the presence of ZnO under UV irradiation, a new, intense emission band emerged at 420 nm, consistent with the formation of 2-hydroxyterephthalic acid and confirming the generation of $^{\bullet}OH$ radicals at the catalyst surface.[49] Furthermore, kinetic measurements performed in the presence of the hydroxyl radical scavenger isopropanol (IPA) revealed a decrease in the apparent rate constant for PNPA hydrolysis from 0.012 $min^{-1}$ to 0.011 $min^{-1}$ under daylight, and from 0.029 $min^{-1}$ to 0.019 $min^{-1}$ under UV irradiation, validating the participation of $^{\bullet}OH$ radicals in the catalytic process (Fig. 7e and d).[50] The minor quenching observed under daylight arises from trace UV components that induce limited photoexcitation of ZnO, whereas the pronounced decrease under UV exposure confirms that the hydrolysis of PNPA proceeds predominantly through a photoinduced radical-mediated pathway.

### 3.4 Mechanistic investigation of PNPA hydrolysis under UV exposure

The mechanistic pathway for ester hydrolysis over ZnO-based nanocatalysts is strongly dependent on the irradiation conditions. Under ambient daylight conditions, the reaction proceeds predominantly through a surface-mediated Lewis acid–base mechanism. In this pathway, surface $Zn^{2+}$ centres act as Lewis acidic sites that coordinate with and polarize the ester carbonyl group, thereby enhancing its electrophilicity. Simultaneously, surface hydroxyl groups (Zn–OH) or adsorbed water molecules function as nucleophiles, facilitating the hydrolytic cleavage of the ester bond. In contrast, under UV irradiation, the mechanism shifts toward a radical-mediated pathway. Photoexcitation of ZnO generates electron–hole ($e^{-}/h^{+}$) pairs, which participate in surface redox reactions leading to the formation of reactive oxygen species such as hydroxyl radicals ($^{\bullet}OH$) and superoxide radicals ($^{\bullet}O_2^{-}$). The formation of these reactive species induces local surface polarisation, arising from charge redistribution around $Zn^{2+}$ centres, which increases their Lewis acidity and strengthens electrostatic interactions with polar PNPA molecules. This enhanced polarity promotes favourable substrate adsorption and molecular orientation at the catalytic interface, facilitating effective bond activation. Simultaneously, photo-induced charge transfer between the excited ZnO surface and the adsorbed PNPA molecule leads to electronic polarisation of the carbonyl group, through coordination to Lewis-acidic $Zn^{2+}$ centres. Thereby rendering the carbonyl carbon more electrophilic and susceptible to nucleophilic attack by either surface-bound –OH or $^{\bullet}OH$ radicals. In addition, surface hydroxyl groups (-OH) contribute synergistically by acting as

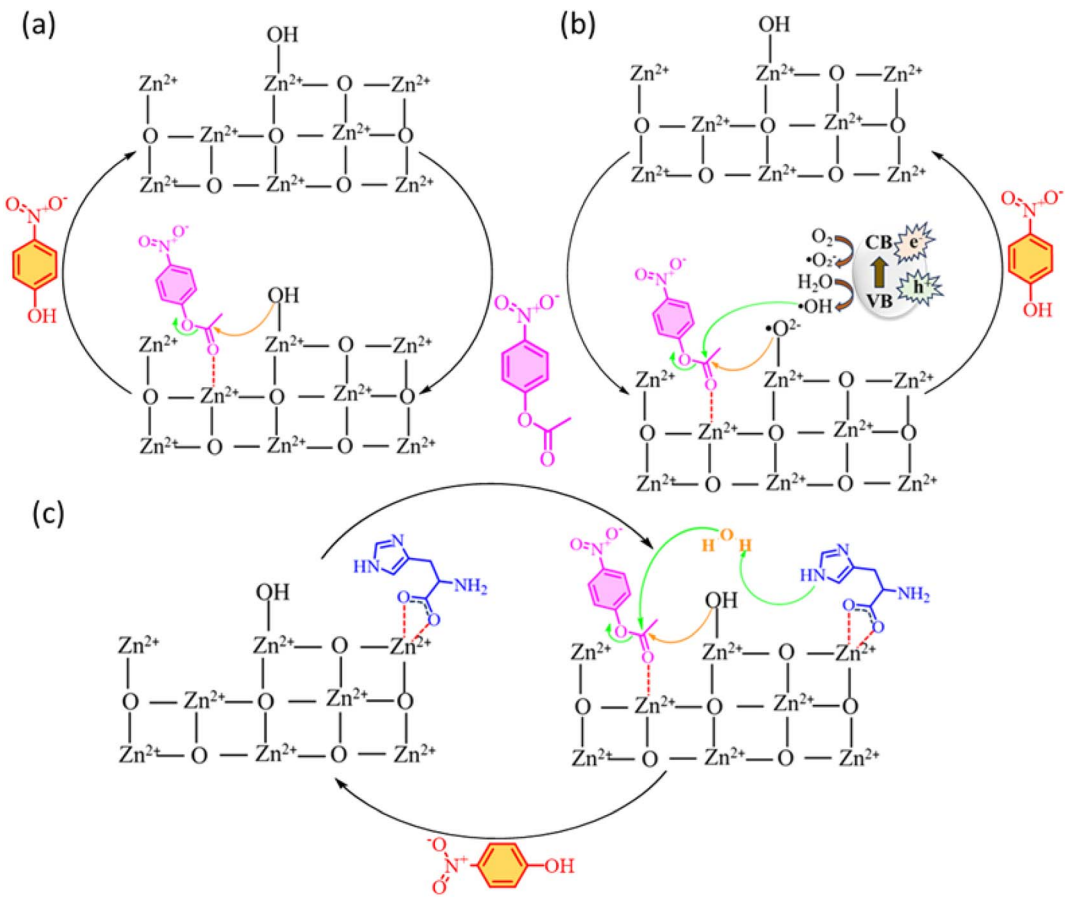


Fig. 8 Proposed mechanism for the catalytic hydrolysis of PNPA in the presence of (a) ZnO-300 (b) ZnO-300 under UV light irradiation (c) ZnO-Histidine.

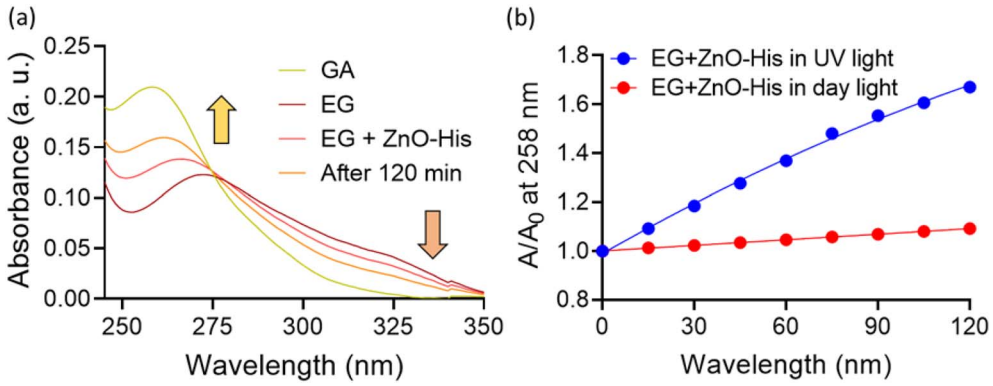


Fig. 9 (a) Spectroscopic monitoring of ethyl gallate (EG) hydrolysis catalysed by the ZnO-His under UV light irradiation. (b) Change in absorbance at 258 nm, hydrolysis of Ethyl Gallate by ZnO-His with and without UV irradiation at pH 7.4 in buffered medium.

both anchoring and reactive sites, stabilising transition states and intermediates *via* hydrogen bonding. In ZnO-His, these effects are further intensified as histidine coordination enhances charge separation, increases surface hydrophilicity, and the imidazole group assists proton transfer, resulting in superior photocatalytic efficiency compared to pristine ZnO-300. Overall, the results reveal that light-driven charge dynamics coupled with histidine-mediated surface modulation transform ZnO-300 into a highly efficient photoactive catalyst capable of accelerating ester bond cleavage with remarkable efficiency (Fig. 8a–c).[51–57]

## 4. Application of the catalyst for gallate ester hydrolysis

Ethyl gallate (EG) is an ester derivative of gallic acid widely used as an antioxidant in food, cosmetic, and pharmaceutical formulations. Its functional performance is governed by hydrolytic cleavage, which releases gallic acid (GA) as the active species. This transformation significantly influences its biological activity, including antioxidant and anti-inflammatory properties, as well as its environmental fate. Conversion of the hydrophobic ester into the more water-soluble gallic acid enhances biodegradability, underscoring the importance of controlled hydrolysis in both biological and applied systems.[58,59] The catalytic performance of the ZnO-His nanocatalyst toward EG hydrolysis was evaluated in aqueous buffer (pH 7.4) under UV irradiation. The progress of the reaction was monitored spectrophotometrically over 120 min. As shown in Fig. 9a, EG exhibited a characteristic absorption maximum at 273 nm, whereas GA showed a more intense, slightly blue-shifted band at 258 nm in buffered medium. Upon addition of ZnO-His to the EG solution under UV light, a gradual decrease in absorbance at 273 nm, accompanied by a concomitant increase at 258 nm, was observed. This spectral transition indicates the progressive conversion of EG to GA, confirming effective catalytic hydrolysis under photoirradiation.[60,61]

Product formation was further verified by ESI-MS analysis (Fig. S10), which revealed a prominent molecular ion peak at $m/z = 170.8$ $[M + H]^+$, consistent with gallic acid. The time-dependent absorbance plot at 258 nm (Fig. 9b) demonstrated a steady increase under UV irradiation, following apparent pseudo-first-order kinetics. In contrast, negligible changes were observed under daylight conditions, indicating minimal catalytic activity in the absence of UV light. Overall, experimental results establish that ZnO-His efficiently catalyzes the hydrolytic cleavage of ethyl gallate under UV irradiation. The catalyst exhibits good activity and stability in aqueous medium, highlighting its potential for light-assisted catalytic transformations and environmentally sustainable applications.

## 5. Conclusion

In summary, a systematic investigation was undertaken to elucidate the structure–property-activity relationship of ZnO nanocatalysts synthesised *via* a facile co-precipitation route and thermally modulated at different calcination temperatures. The results revealed that temperature critically influences the physicochemical and morphological properties of ZnO, with low-temperature calcination (300 °C) yielding smaller crystallites, higher surface area, and a distinctive 3D nanoflake morphology rich in surface hydroxyl groups, whereas high-temperature calcination at 700 °C led to the formation of larger crystallites with a compact 3D polyhedral structure and reduced surface hydroxylation. These features resulted in ZnO-300 with a significantly higher reaction rate in the hydrolysis of *p*-nitrophenyl acetate (PNPA) than ZnO-700, confirming that enhanced surface defects and hydroxyl functionalities at lower calcination temperatures promote superior catalytic activity. Functional modification of ZnO-300 with histidine further enhanced catalytic performance through synergistic Lewis acid-Brønsted base bifunctionality. Spectroscopic analyses confirmed that histidine coordination effectively modulates the surface charge environment, increases hydrophilicity, and suppresses surface defects without disrupting the wurtzite ZnO lattice. Under UV illumination, both ZnO-300 and ZnO-His exhibited pronounced photoactivation, with ZnO-His showing a substantially faster reaction rate compared to its unmodified counterpart. This enhancement arises from the synergistic interplay of photoinduced charge separation and histidine-

mediated proton transfer, which cumulatively promote the generation of reactive ˙OH radicals and facilitate a radical-mediated pathway for efficient ester bond cleavage. Kinetic studies established that the catalytic reaction follows pseudo-first-order and Michaelis–Menten-type kinetics, while recyclability tests confirmed the structural robustness and reusability of ZnO-300 over multiple cycles. Taken together, these findings demonstrate that controlled thermal treatment and molecular-level surface modification are powerful strategies for tuning the catalytic and photoresponsive properties of ZnO nanostructures. Further, the ZnO-His was used for UV mediated, room temperature catalysis of an emerging contaminant, ethyl gallate. The formation of hydrolysed product was evident through changes in absorption spectrum as well as ESI-MS mass spectral analysis.

## Auther contributions

Swapan Patra: writing – original draft, visualization, validation, methodology, investigation. Sounak Roy: methodology, writing – original draft, visualization, validation, supervision, software. Nilanjan Dey: writing-review & editing, supervision, resources, project administration, investigation, funding acquisition, formal analysis, conceptualization.

## Conflicts of interest

There are no conflicts to declare.

## Data availability

Data will be made available on request.

Supplementary information: experimental details, UV-visible spetra of ZnO-300, ZnO-700, and ZnO-His, XPS survey spectra of ZnO-300 and ZnO-700, XRD spetra, ESI-MS spectra, Raman spectra of ZnO-300 and ZnO-700. See DOI: https://doi.org/10.1039/d6su00100a.

## Acknowledgements

ND thanks VB Ceramic Consultants for financial support and a fellowship to SP. The authors thank the BITS Pilani Hyderabad campus for technical support. SR thanks thank the BITS Pilani Hyderabad campus for technical support.

## References

1 M. R. Ahmad, A. A. Ansari, M. Dhayal and R. Lv, Bandgap engineering of ZnO nanomaterials for enhanced electrochemical and photocatalytic efficiency, *Renew. Sustain. Energy Rev.*, 2025, **219**, 115767.
2 W. Jing, Y. Xia, Y. Dong, R. Chen, L. Xiang and S. Komarneni, Defect-rich ZnO nanosheets of high surface area as an efficient visible-light photocatalyst, *Appl. Catal., B*, 2016, **192**, 8–16.
3 S. Patra and N. Dey, From Solution to Paper-Immobilized Heterogeneous Interface: Molecularly Engineered Amphiphilic Imidazole Catalysts Mimicking Hydrolase Activity via Tunable Supramolecular Microenvironments, *J. Environ. Chem. Eng.*, 2026, 121325.
4 J.-T. Du, Q. Sun, X.-F. Zeng, D. Wang, J.-X. Wang and J.-F. Chen, ZnO nanodispersion as pseudohomogeneous catalyst for alcoholysis of polyethylene terephthalate, *Chem. Eng. Sci.*, 2020, **220**, 115642.
5 S. Cao, F. F. Tao, Y. Tang, Y. Li and J. Yu, Size- and shape-dependent catalytic performances of oxidation and reduction reactions on nanocatalysts, *Chem. Soc. Rev.*, 2016, **45**, 4747–4765.
6 G. Y. Wang, W. X. Zhang, H. L. Lian, D. Z. Jiang and T. H. Wu, Effect of calcination temperatures and precipitant on the catalytic performance of Au/ZnO catalysts for CO oxidation at ambient temperature and in humid circumstances, *Appl. Catal., A*, 2003, **239**, 1–10.
7 A. Alwash, Impact of Calcination Temperature on the Structural and Photocatalytic Properties of ZnO Synthesized from Gum Arabic for Methylene Blue Dye Removal, *J. Hazard. Mater. Adv.*, 2025, **17**, 100625.
8 L. Chen, Y. Cui, Z. Xiong, M. Zhou and Y. Gao, Chemical functionalization of the ZnO monolayer: structural and electronic properties, *RSC Adv.*, 2019, **9**, 21831–21843.
9 A. S. H. H. Hameed, G. Louis, C. Karthikeyan, N. Thajuddin and G. Ravi, Impact of l-Arginine and l-Histidine on the structural, optical and antibacterial properties of Mg doped ZnO nanoparticles tested against extended-spectrum beta-lactamases (ESBLs) producing Escherichia coli, *Spectrochim. Acta, Part A*, 2019, **211**, 373–382.
10 S. Payra, S. K. Ganeshan, S. Challagulla and S. Roy, A correlation story of syntheses of ZnO and their influence on photocatalysis, *Adv. Powder Technol.*, 2020, **31**, 510–520.
11 S. Payra, S. Challagulla, Y. Bobde, C. Chakraborty, B. Ghosh and S. Roy, Probing the photo- and electro-catalytic degradation mechanism of methylene blue dye over ZIF-derived ZnO, *J. Hazard. Mater.*, 2019, **373**, 377–388.
12 E. Lizundia, L. Ruiz-Rubio, J. L. Vilas and L. M. León, Towards the development of eco-friendly disposable polymers: ZnO-initiated thermal and hydrolytic degradation in poly(L-lactide)/ZnO nanocomposites, *RSC Adv.*, 2016, **6**, 15660–15669.
13 R. E. Adam, G. Pozina, M. Willander and O. Nur, Synthesis of ZnO nanoparticles by co-precipitation method for solar driven photodegradation of Congo red dye at different pH, *Photon. Nanostruct.*, 2018, **32**, 11–18.
14 A. Shchelokov, N. Palko, V. Potemkin, M. Grishina, R. Morozov, E. Korina, D. Uchaev, I. Krivtsov and O. Bol'shakov, Adsorption of native amino acids on nanocrystalline $TiO_2$: Physical chemistry, QSPR, and theoretical modeling, *Langmuir*, 2018, **35**, 538–550.
15 A. Prabhu, P. C. Meenu and S. Roy, Creation of a facile heterojunction in Co/ZnO–$TiO_2$ for the photocatalytic degradation of alizarin S, *New J. Chem.*, 2024, **48**, 10552–10562.
16 G. Ravi and K. Thyagarajan, Impact of calcination temperature on the structural, surface area, and magnetic

 

properties of NiFe2O4/MnFe2O4/CeO2 ternary nanocomposites, *Inorg. Chem. Commun.*, 2025, **174**, 114028.
17 I. Riwayati, S. Winardi, S. Madhania and M. Shimada, Green synthesis of ZnO nanoparticles using cosmos caudatus: effects of calcination temperature and precursor type on photocatalytic and antimicrobial activities, *Res. Eng.*, 2024, **24**, 103594.
18 S. Payra, S. K. Ganeshan, S. Challagulla and S. Roy, A correlation story of syntheses of ZnO and their influence on photocatalysis, *Adv. Powder Technol.*, 2020, **31**, 510–520.
19 S. Gandhi, R. Kaur, V. Sharma and S. K. Mandal, Effect of calcination temperature on the morphology and catalytic properties of ZnO nanostructures fabricated from a chiral precursor for photodegradation of both cationic and anionic dyes, *New J. Chem.*, 2022, **46**, 3645–3657.
20 P. C. Meenu, S. Roy, C. Chakraborty and S. Roy, Electro catalytic oxidation reactions for harvesting alternative energy over non noble metal oxides: Are we a step closer to sustainable energy solution?, *Adv. Powder Technol.*, 2021, **32**, 2663–2689.
21 M. R. Parra and F. Z. Haque, Aqueous chemical route synthesis and the effect of calcination temperature on the structural and optical properties of ZnO nanoparticles, *J. Mater. Res. Technol.*, 2014, **3**, 363–369.
22 V. N. Jafarova and G. S. Orudzhev, Structural and electronic properties of ZnO: A first-principles density-functional theory study within LDA (GGA) and LDA (GGA)+U methods, *Solid State Commun.*, 2021, **325**, 114166.
23 K. Lee, Y.-G. Lu, C.-H. Chuang, J. Ciston and G. Dukovic, Synthesis and characterization of (Ga1−xZnx)(N1−xOx) nanocrystals with a wide range of compositions, *J. Mater. Chem. A*, 2016, **4**, 2927–2935.
24 X. Li, Y. Wang, W. Liu, G. Jiang and C. Zhu, Study of oxygen vacancies' influence on the lattice parameter in ZnO thin film, *Mater. Lett.*, 2012, **85**, 25–28.
25 J. Yang, Z. Wang, W. Xiao, Y. Peng, M. Qiu, X. Xiong, Y. Lu, T. Chen and Z. Xu, Zn(II)-complex-based hydrolytic nanozymes prepared by nanoprecipitation for the hydrolysis of carboxylic esters and methyl parathion, *Colloids Surf., A*, 2023, **675**, 132034.
26 F. G. Svensson, E. Djurberg, S. Kim, G. Westin and L. Österlund, Effect of surface impurities and lattice defects on the photocatalytic activity of ZnO nanoparticles, *Langmuir*, 2025, **41**, 28399–28410.
27 P. Bernard, P. Stelmachowski, P. Broś, W. Makowski and A. Kotarba, Demonstration of the influence of specific surface area on reaction rate in heterogeneous catalysis, *J. Chem. Educ.*, 2021, **98**, 935–940.
28 N. Scholz, Ecotoxicity and biodegradation of phthalate monoesters, *Chemosphere*, 2003, **53**, 921–926.
29 M. Takahashi, I. Hirota, T. Nakano, T. Kotani, D. Takani, K. Shiratori, Y. Choi, M. Haba and M. Hosokawa, Effects of steric hindrance and electron density of ester prodrugs on controlling the metabolic activation by human carboxylesterase, *Drug Metab. Pharmacokinet.*, 2021, **38**, 100391.
30 D. I. Kreller, G. Gibson, W. Novak, G. W. Van Loon and J. H. Horton, Competitive adsorption of phosphate and carboxylate with natural organic matter on hydrous iron oxides as investigated by chemical force microscopy, *Colloids Surf., A*, 2003, **212**, 249–264.
31 E. S. Pereira, J. C. S. Da Silva, T. A. S. Brandão and W. R. Rocha, Phosphorane lifetime and stereo-electronic effects along the alkaline hydrolysis of phosphate esters, *Phys. Chem. Chem. Phys.*, 2016, **18**, 18255–18267.
32 P. Bernard, P. Stelmachowski, P. Broś, W. Makowski and A. Kotarba, Demonstration of the influence of specific surface area on reaction rate in heterogeneous catalysis, *J. Chem. Educ.*, 2021, **98**, 935–940.
33 I. Bose and Y. Zhao, Selective hydrolysis of aryl esters under acidic and neutral conditions by a synthetic aspartic protease mimic, *ACS Catal.*, 2021, **11**, 3938–3942.
34 A. Gayen, T. Baidya, K. Biswas, S. Roy and M. S. Hegde, Synthesis, structure and three-way catalytic activity of Ce1−xPtx/2Rhx/2O2−δ (x = 0.01 and 0.02) nanocrystallites: Synergistic effect in bimetal ionic catalysts, *Appl. Catal., A*, 2006, **315**, 135–146.
35 P. Chauhan, A. Sarkar and M. Ravikanth, Synthesis of Ni(II) and Zn(II) complexes of pyrrolyl dipyrrins and their biomimetic role in catalyzing the hydrolysis of the phospho-ester bond, *Dalton Trans.*, 2026, **55**, 1349–1359.
36 S. Patra, D. Singh and N. Dey, Divergent binding modes direct functional modulation: toward next-generation ionic liquids for enzyme stabilization and biocatalysis, *RSC Sustainability*, 2026, **4**, 803–812.
37 E. Roduner, Understanding catalysis, *Chem. Soc. Rev.*, 2014, **43**, 8226–8239.
38 X. Cui, Y. Wang, G. Jiang, Z. Zhao, C. Xu, A. Duan, J. Liu, Y. Wei and W. Bai, The encapsulation of CdS in carbon nanotubes for stable and efficient photocatalysis, *J. Mater. Chem. A*, 2014, **2**, 20939–20946.
39 T. Kamsuwan, A. Guntida, P. Praserthdam and B. Jongsomjit, Differences in deterioration behaviors of Cu/ZnO/Al2O3 catalysts with different Cu contents toward hydrogenation of CO and CO2, *ACS Omega*, 2022, **7**, 25783–25797.
40 C. Fan, Y. Tang, H. Wang, Y. Huang, F. Xu, Y. Yang, Y. Huang, W. Rong and Y. Lin, ZIF-90 with biomimetic Zn–N coordination structures as an effective nanozyme to mimic natural hydrolase, *Nanoscale*, 2022, **14**, 7985–7990.
41 M. Anbuvannan, M. Ramesh, G. Viruthagiri, N. Shanmugam and N. Kannadasan, Synthesis, characterization and photocatalytic activity of ZnO nanoparticles prepared by biological method, *Spectrochim. Acta, Part A*, 2015, **143**, 304–308.
42 S. Mahakal, H. M. Pathan, M. Prasad, S. Rondiya, S. P. Patole and S. R. Jadkar, Modification in toxicity of l-histidine-incorporated ZnO nanoparticles toward *Escherichia coli*, *ACS Omega*, 2023, **8**, 34354–34363.
43 K. S. Suganthi and K. S. Rajan, Temperature induced changes in ZnO–water nanofluid: zeta potential, size distribution and viscosity profiles, *Int. J. Heat Mass Transfer*, 2012, **55**, 7969–7980.

44 A. Sola-Rabada, M.-K. Liang, M. J. Roe and C. C. Perry, Peptide-directed crystal growth modification in the formation of ZnO, *J. Mater. Chem. B*, 2015, **3**, 3777–3788.

45 M. M. H. Farooqi and R. K. Srivastava, Enhanced UV–vis photoconductivity and photoluminescence by doping of samarium in ZnO nanostructures synthesized by solid state reaction method, *Optik*, 2016, **127**, 3991–3998.

46 S. Mahakal, H. M. Pathan, M. Prasad, S. Rondiya, S. P. Patole and S. R. Jadkar, Modification in toxicity of l-histidine-incorporated ZnO nanoparticles toward *Escherichia coli*, *ACS Omega*, 2023, **8**, 34354–34363.

47 K.-Y. Wang, J. Zhang, Y.-C. Hsu, H. Lin, Z. Han, J. Pang, Z. Yang, R.-R. Liang, W. Shi and H.-C. Zhou, Bioinspired framework catalysts: From enzyme immobilization to biomimetic catalysis, *Chem. Rev.*, 2023, **123**, 5347–5420.

48 C. Yang, Q. Li, L. Tang, K. Xin, A. Bai and Y. Yu, Synthesis, photocatalytic activity, and photogenerated hydroxyl radicals of monodisperse colloidal ZnO nanospheres, *Appl. Surf. Sci.*, 2015, **357**, 1928–1938.

49 D. Biswakarma, N. Dey and S. Bhattacharya, Hydrogel nanocomposite towards optical sensing of spermine in biomedical and real-life food samples and remediation of toxic dyes from wastewater, *Langmuir*, 2023, **39**, 11610–11620.

50 Z. Chen, Y. Teng, W. Wang, R. Hong, L. Huang, X. Wang, F. Zhu, *et al.*, Enhanced UV photoreductive destruction of perfluorooctanoic acid in the presence of alcohols: Synergistic mechanism of hydroxyl radical quenching and solvent effect, *Appl. Catal., B*, 2022, **316**, 121652.

51 S. Velusamy, A. Roy, E. Mariam, S. Krishnamurthy, S. Sundaram and T. K. Mallick, Effectual visible light photocatalytic reduction of para-nitro phenol using reduced graphene oxide and ZnO composite, *Sci. Rep.*, 2023, **13**, 9521.

52 P. K. R. Boppidi, P. Raj, S. Challagulla, S. R. Gollu, S. Roy, S. Banerjee and S. Kundu, Unveiling the dual role of chemically synthesized copper doped zinc oxide for resistive switching applications, *J. Appl. Phys.*, 2018, **124**, 214901.

53 Q. Raza, I. Bibi, F. Majid, A. Dahshan, S. Kamal, K. Jilani, G. Fatima, B. Taj, N. Alwadai and M. Iqbal, Dielectric, ferroelectric, optical and photocatalytic properties of Al and Ag-doped strontium hexaferrite ($SrFe_{12}O_{19}$) synthesized via facile micro-emulsion approach, *J. Alloys Compd.*, 2024, **985**, 174098.

54 Q. Raza, I. Bibi, F. Majid, S. Kamal, S. Ata, A. Ghafoor, M. I. Arshad, S. H. Al-Mijalli, A. Nazir and M. Iqbal, Solar light-based photocatalytic removal of CV and RhB dyes using Bi and Al doped $SrFe_{12}O_{19}$ NPs and antibacterial properties, *J. Ind. Eng. Chem.*, 2023, **118**, 469–482.

55 Q. Raza, S. Iqbal, T. N. Tamin, A. Fareed, W. A. Al-onazi, M. S. Elshikh, R. Iqbal and M. Jamshaid, Heterostructured $SrFe_{12}O_{19}$@g-$C_3N_4$ nanocomposites applied to linezolid antibiotic degradation under visible-induced catalytic process, *J. Sol-Gel Sci. Technol.*, 2025, **113**, 534–547.

56 Q. Raza, S. Iqbal, F. Bibi, E. Aldosari, A. Kalsoom, M. Jamshaid, R. Iqbal and S. Lim, A novel g-$C_3N_4$-based $CeO_2$ loaded ternary $CeO_2$/$CoFe_2O_4$@g-$C_3N_4$ heterojunction catalyst for the efficient removal of enrofloxacin from veterinary wastewater, *J. Sol-Gel Sci. Technol.*, 2025, **114**, 532–548.

57 Q. Raza, G. Fatima, B. Lu, I. Bibi, J. An and S. Lim, In situ synthesis and synergistic effect of Ag/Al@$SrFe_{12}O_{19}$ decorated with graphitic carbon nitride: mechanistic insight into photocatalytic and antimicrobial activity, *Surf. Interfaces*, 2025, 107203.

58 F.-L. Hsu, P.-S. Chen, H.-T. Chang and S.-T. Chang, Effects of alkyl chain length of gallates on their antifungal property and potency as an environmentally benign preservative against wood-decay fungi, *Int. Biodeterior. Biodegrad.*, 2009, **63**, 543–547.

59 Q. Wang, X. Wang, D. Cai, J. Yu, X. Chen, W. Niu, S. Wang, X. Liu, D. Zhou and F. Yin, Hydrolysis and transport characteristics of phospholipid complex of alkyl gallates: potential sustained release of alkyl gallate and gallic acid, *J. Agric. Food Chem.*, 2024, **72**, 2145–2153.

60 H. V. Barkale and N. Dey, Functionalized cyanostilbene-based nano-AIEgens: multipoint binding interactions for improved sensing of gallic acid in real-life food samples, *J. Mater. Chem. B*, 2024, **12**, 8746–8756.

61 I. Melikhov, M. Bacher, T. Hosoya, H. Hettegger, A. Potthast and T. Rosenau, On the chemical fate of propyl gallate as stabilizer in Lyocell spinning dopes, *Cellulose*, 2023, **30**, 5373–5390.